11th International Symposium on Turbulence and Shear Flow Phenomena (TSFP11)
Southampton, UK, July 30 to August 2, 2019

EFFECT OF DBD PLASMA ACTUATORS ON VORTICAL STRUCTURES IN A TURBULENT MIXING LAYER

Srikar Yadala[1,2,*], **Nicolas Benard**[1], **Marios Kotsonis**[2], **Franck Kerherve**[1], **Eric Moreau**[1]

[1] Institut PPrime, Université de Poitiers (CNRS UPR 3346, ISAE-ENSMA)
Boulevard Marie et Pierre Curie, BP 30179, 86962 Futuroscope, France
[*] srikar.yadala.venkata@univ-poitiers.fr

[2] AWEP Department, Section of Aerodynamics
Delft Univeristy of Technology
Kluyverweg 1, 2629HS Delft, The Netherlands

ABSTRACT

The influence of linear (spanwise-uniform) forcing applied by a DBD plasma actuator on the growth of a turbulent mixing layer and the dynamics of large-scale spanwise vortices, are investigated experimentally. Furthermore, the freestream turbulence intensity in the low-velocity stream is maintained at a high level to examine its impact on the control-authority of the applied forcing. The influence of the applied forcing on the dynamics and interactions of the spanwise vortices in the mixing layer is apparent. However, the growth rate of the mixing layer is not affected, suggesting that the high level of freestream turbulence diminishes the control-authority of the applied forcing.

1 INTRODUCTION

The study of flow characteristics in a turbulent mixing layer is very significant for practical aerodynamics. Such a flow arrangement governs the rate of mixing in combustion chambers, flow in jets and wakes among others. It is also a major source of broadband noise associated with jet propulsion. Furthermore, flow over modern aircraft wings is dominated by complex interactions between free-shear flows. A plane mixing layer is the simplest representation of a free-shear flow that attains a self-similar state (Brown & Roshko, 1974; Oster & Wygnanski, 1982). Thus, understanding and devising methods to control the structures and growth of a plane mixing layer is instrumental towards improving the performance of many aero-thermo-dynamic systems.

The interaction of two parallel streams with different freestream velocity gives rise, at the trailing-edge of a splitter plate, to a plane mixing layer. Such a flow field is characterised by large-scale, spanwise (coherent) vortices that arise from the Kelvin-Helmholtz (primary) instability (Brown & Roshko, 1974). The amalgamation of subsequent spanwise vortices, or vortex pairing, has a significant influence on the growth of the mixing layer (Oster & Wygnanski, 1982). Sub-harmonic frequencies of the most-amplified Kelvin-Helmholtz instability, forming immediately downstream of the splitter plate, act as catalyst to the pairing process and hence are observed to control the growth of the mixing layer (Ho & Huang, 1982). However, the development of a mixing layer is highly sensitive to initial conditions, especially to freestream turbulence intensity in the low-velocity stream (Chandrsuda *et al.*, 1978; Pui & Gartshore, 1979). Pui & Gartshore (1979) observed that a high level of turbulence in the low-velocity stream leads to higher Reynolds stresses and growth rates. In such flow conditions, due to the early induction of three-dimensionality, the strength and coherence of the two-dimensional vortices decreases, eventually resulting in their breakdown due to helical vortex pairing (Chandrsuda *et al.*, 1978).

In the current research, the effect of linear (spanwise-uniform) electro-fluid-dynamic (EFD) forcing exerted by a dielectric barrier discharge (DBD) plasma actuator on the coherent vortices in a mixing layer and the subsequent pairing process is investigated experimentally. A thorough review on the basic principles and working mechanism of these actuators is synthesized in Benard & Moreau (2014). DBD actuators have found many successful boundary layer flow control applications for instability control and turbulent drag reduction. However, in contrast to laminar/transitional and wall-bounded flow configurations, previous work on application of DBD actuators in turbulent mixing layers is very limited (Ely & Little, 2013). Additionally, the low-velocity stream is maintained at a high level of freestream turbulence intensity, to study its impact on the effectiveness of the applied forcing. This is necessary as such a flow configuration is more common in practical engineering applications.

2 EXPERIMENTAL SET-UP

The experiments were carried out in a closed-loop wind-tunnel, specially modified to accommodate mixing layer studies. The dimensions of the test-section are 30 cm $\times$ 30 cm $\times$ 1.2 m in height, width and length respectively. A 15 mm thick aluminium (splitter) plate is installed to generate two parallel streams. In order to realize a difference in the velocity and turbulence intensity between the two streams, an opportune combination of foams and metallic grids were installed in the bottom (i.e. low-velocity) stream, at the entrance of the convergence located just upstream of the test section. For the entire experiment, the freestream velocity of the bottom and top flow streams were

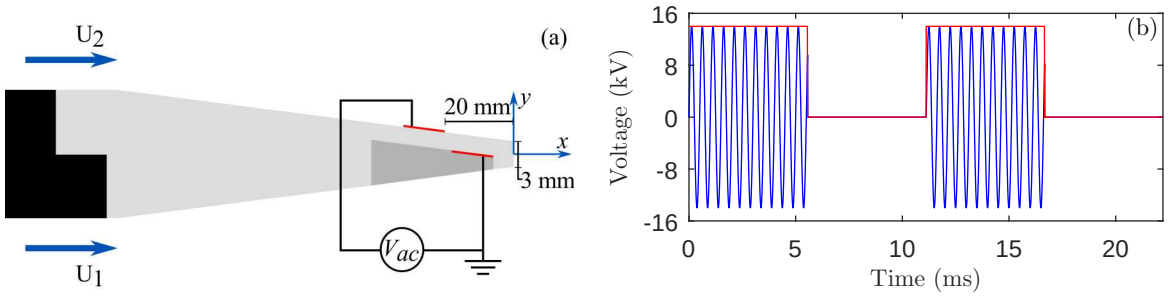

Figure 1: (a) Splitter-plate edge design (not to scale). The aluminium plate (black), the PMMA splitter-plate edge (light gray), the electrodes (red lines) and the epoxy resin encapsulating the grounded electrode (dark gray) is shown. The reference system is also depicted. (b) Sample input waveform (blue) and square-wave burst modulation (red). $V_{ac} = 14$ kV, $f_{ac} = 2$ kHz, $f_b = 90$ Hz.

maintained at $U_1 = 5$ m s^{-1} and $U_2 = 15$ m s^{-1} respectively. This resulted in a velocity ratio of $r = U_1/U_2 = 0.33$. Turbulence intensity measured with a single hot-wire sensor in the low-velocity (bottom) stream was $\overline{Tu}/U_1 = 2.8\%$ and that in the high-velocity (top) stream was $\overline{Tu}/U_2 = 0.13\%$ (bandpass filtered between 1 and 500 Hz). The coordinate system used in this study is represented by xyz where x is along the freestream direction, y is perpendicular to the plane of the mixing layer and z is along the span.

The end of the splitter plate was made with PMMA and has a 120 mm long taper of about 3.1° on both the top and bottom sides, resulting in a 3 mm thick trailing-edge. An opportune incision was made, so as to realize a 2 mm thick PMMA plate which served as the dielectric substrate (see figure 1a). The electrodes of the DBD actuator were uniform strips of aluminium. The air-exposed electrode was 10 mm wide while the second electrode was 15 mm wide. The electrodes were mounted asymmetrically on either side of the dielectric with a relative gap of 3 mm. Ely & Little (2013) observed that the DBD actuator has more control-authority on the mixing layer when the EFD forcing is applied in the high-velocity stream. Thus, in the current experiment, the air-exposed electrode of the DBD actuator was installed on the high-velocity side. The second electrode was installed in the incision which was then filled with an epoxy resin to encapsulate this electrode. This construction resulted in a DBD actuator that exerts a spanwise-uniform EFD force along the freestream direction in the high-velocity stream. The plasma-generating edge of the air-exposed electrode was at $x = -20$ mm. The air-exposed electrode was supplied with the high-voltage AC signal while the encapsulated electrode was grounded. The voltage waveform of the driving signal was sinusoidal with an AC frequency $f_{ac} = 2$ kHz and amplitude $V_{ac} = 14$ kV. Furthermore, a low frequency (f_b) burst modulation (square waveform, 50% duty cycle) was used to excite the mixing layer. A sample of the resulting input signal is depicted in figure 1b.

Phase-locked, high-speed, planar particle image velocity (PIV) was employed for the quantification of the flow field along the $x-y$ directions at mid-span ($z = 0$). Two fields, one in the near-wake region and the other in the far-wake region was captured with this set-up. The final vector spacing is 1.13 mm. The acquisition rate during all the tested cases was 10 kHz in single-frame mode. A sequence of 10,000 images were acquired for every tested flow case. The resulting measurement time was 1 s per test case. Furthermore, in order to achieve a phase-locked measurement, the trigger to initiate the PIV acquisition was synchronized with the driving signal supplied to the DBD actuator.

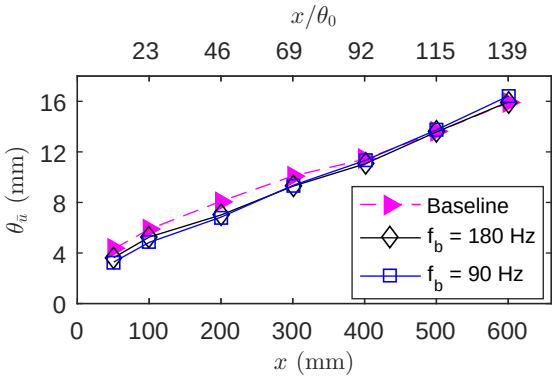

Figure 2: Momentum thickness ($\theta_{\bar{u}}$) of the mixing layer along x.

3 RESULTS

The momentum thickness ($\theta_{\bar{u}}$) is used as a measure of the growth of the mixing layer. It is computed according to equation 1 (Oster & Wygnanski, 1982),

$$\theta_{\bar{u}} = \int_{-\infty}^{\infty} \frac{\bar{u} - U_1}{U_2 - U_1} \left[1 - \frac{\bar{u} - U_1}{U_2 - U_1}\right] dy \qquad (1)$$

where $\bar{u}$ is the longitudinal component of mean velocity obtained from PIV. The momentum thickness of the unforced mixing layer (hereafter referred to as baseline) along the x direction is shown in figure 2. The mixing layer is observed to grow linearly which is in line with previous works (Oster & Wygnanski, 1982; Ho & Huang, 1982). This linear growth can be attributed to vortex pairing occurring stochastically in space and time. It is good to note that the splitter-plate, having a 3 mm thick trailing-edge, generates a recirculation region, as a consequence of which a velocity deficit is observed in the $\bar{u}$-profiles along y. This velocity deficit decreases downstream and the $\bar{u}$ velocity profiles resemble a *tanh* profile downstream of $x = 50$ mm. The momentum thickness of the baseline at this x-location is $\theta_0 = 4.33$ mm. This value is utilized to non-dimensionalise the spatial coordinates hereafter.

The normalized, average u-velocity component ($\bar{u}_N$) of

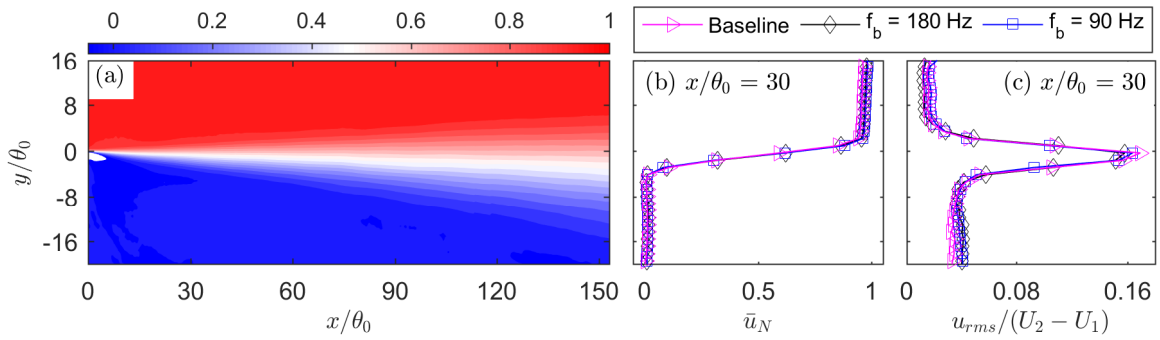

Figure 3: (a) Time-averaged, normalized u-velocity component ($\bar{u}_N$) of the baseline (unforced) case. (b) $\bar{u}_N$ profiles along y at $x/\theta_0 = 30$. (c) Variation of u_{rms} along y at $x/\theta_0 = 30$.

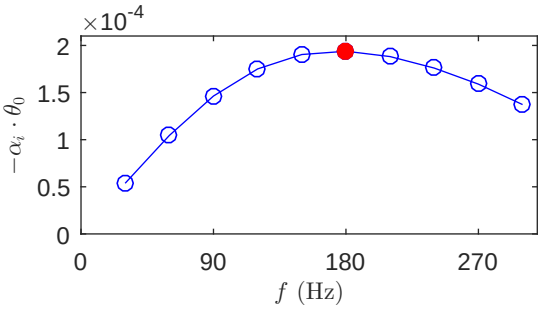

Figure 4: Non-dimensional amplification rate of perturbations at different frequencies computed using LST.

the baseline (unforced mixing layer) is presented in figure 3a. Here, the velocity field is normalized by $\bar{u}_N = (\bar{u} - U_1)/(U_2 - U_1)$. The mixing layer developed at the end of the splitter-plate due to the interaction of the two flow streams is clearly visible. Eventually ($x/\theta_0 > 11$), the mixing layer evolves into a flow that is well approximated by a *tanh* profile as observed in the velocity profile at $x/\theta_0 = 30$, presented in figure 3b. Furthermore, the profile of (normalized) u_{rms} at the same x-location is shown in figure 3c. As expected, the fluctuations are highest within the mixing layer. However, the fluctuations in the low-velocity stream are higher compared to that in the high-velocity flow stream which is a direct result of higher level of turbulence in the low-velocity stream.

Although the low-velocity stream is turbulent, the high value of shear in the time-averaged flow gives ground for the use of linear stability theory (LST) to determine the fundamental (most amplified) frequency (f_0) of perturbations arising from the inviscid Kelvin-Helmholtz instability mechanism in the mixing layer. To do this, a *tanh* profile is fit to the u-velocity profile at $x = 50$ mm obtained from PIV. The spatial growth rate (or wave number) is then obtained by solving the Rayleigh equation (Michalke, 1965) with the Chebyshev collocation method, using 400 polynomials. From this, the fundamental frequency of the current mixing layer configuration is identified to be $f_0 = 180$ Hz (red dot in figure 4). The corresponding wavelength of the fundamental instability wave is $\lambda_0/\theta_0 = 12.8$ ($\lambda_0 = 55.5$ mm).

The mixing layer is now forced with the DBD plasma actuator to impart perturbations at $f_b = f_0 = 180$ Hz and its sub-harmonic $f_b = f_0/2 = 90$ Hz, in order to investigate the effect of these perturbations. The normalized $\bar{u}_N$-velocity profile of the forced mixing layers at $x/\theta_0 = 30$ is shown in figure 3b. The curves still resemble a *tanh* profile. In addition, the profiles of both cases are observed to almost collapse on to that of the baseline. The same is observed in the profile of the u_{rms} presented in figure 3c. However, the similarity in u_{rms} could be because, while the forcing redistributes the energy in the different frequency bands of the spectra, it does not affect the total spectral energy in the mixing layer (Oster & Wygnanski, 1982).

The momentum thickness of the forced mixing layers along x are presented in figure 2 as well. As witnessed in the velocity profiles, no significant change in the growth of mixing layer is observed due to forcing when compared to the baseline (at least in the measured domain). The differences in $\theta_{\bar{u}}$ seen between the different cases are comparable to the measurement error of the PIV system, therefore no conclusive remarks can be made. This is contradictory to previous works on forced mixing layers (Ho & Huang, 1982; Oster & Wygnanski, 1982; Ely & Little, 2013) where a significant difference was observed. These results suggest that the EFD forcing exerted by the current DBD plasma actuator seems to have no control-authority on the mixing layer when compared to previous research efforts. This could be due to the high level of turbulence in the low-velocity stream (compared to 0.2% of turbulence intensity in Oster & Wygnanski (1982) for instance). However, a thorough investigation of the ensuing flow field is necessary before making any conclusion.

In order to gain more insight into the effect of the unsteady low-frequency forcing, the spatial organisation of these fluctuating fields is sought. Proper orthogonal decomposition (POD) was applied on the full set of PIV vector fields using the snapshot technique (Sirovich, 1987). Previous works have applied POD on experimental data obtained from hot-wire measurements of the mixing layer. Rajaee *et al.* (1994) applied POD to velocity measurements in a forced mixed layer. The forcing was applied by acoustic means. The input signal was composed of two superimposed sine waves, one with the frequency of the fundamental instability in the mixing layer and the other its subharmonic. They found that the first two POD spatial modes represent structures pertaining to the sub-harmonic instability while the following two (modes 3 and 4) represent structures of the fundamental instability.

In the current work, POD was applied on both fields separately to analyse the effect of the forcing in the near-wake and far-wake regions. The first two empirical POD eigenfunctions (or spatial modes) are quarter-wave trans-

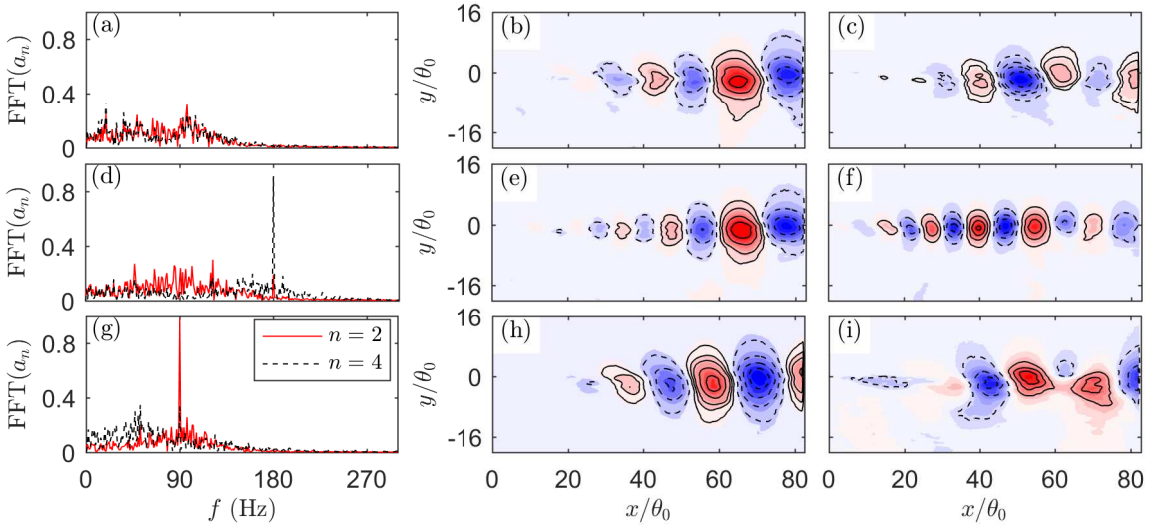

Figure 5: Near-wake POD plots. (a) FFT of the temporal coefficients (a_n) of pair 1-2 ($a_{n=2}$) and pair 3-4 ($a_{n=4}$) of the baseline. (b) and (c) show the vertical component of the corresponding eigenfunctions $\Phi_v^{n=2}$ and $\Phi_v^{n=4}$ respectively (blue, dashed line - negative; red, solid line - positive). (d), (e) and (f) are the same as the first three plots but for the case when the mixing layer is forced at $f_b = 180$ Hz. (g), (h) and (i) are for the case when the mixing layer is forced at $f_b = 90$ Hz.

lates of each other in the streamwise direction which is a natural outcome of the POD procedure on the flow. The same is true with the third and fourth modes as well. Hence, only the results pertaining to the FFT of the temporal coefficients (a_n) and the corresponding vertical component of the eigenfunctions (Φ_v^n), of the second and fourth POD modes are presented here.

The POD results pertaining to the near-wake region of the baseline and both forcing cases are presented in figure 5. In the baseline case, the FFT indicates fluctuations below the fundamental frequency (figure 5a). When the mixing layer is forced at the fundamental frequency, no peak in the FFT is observed in the first pair of POD modes (pair 1-2) while a clear peak is observed at the forcing frequency ($f_b = 180$ Hz) in the second pair (pair 3-4) as seen in figure 5d. While, when sub-harmonic forcing is applied (figure 5g), a significant peak is observed in the FFT at the forced frequency ($f_b = 90$ Hz) in pair 1-2 but a rather weak peak is observed in pair 3-4. Even though the mixing layer is excited at these frequencies separately, unlike in the experiments of Rajaee *et al.* (1994), these results corroborate well with their observations. Additionally, these results demonstrate the influence of the applied forcing on the mixing layer.

When the mixing layer is forced at $f_b = 180$ Hz, structures are observed in the eigenfunctions of both the first and second pairs of POD modes. The structures in pair 3-4 (figure 5f) are smaller in size and have smaller wavelengths compared to those in the baseline (figure 5c), thus confirming the effect of the applied forcing on these fluctuations. These structures orient themselves with an obtuse angle with the streamwise direction initially, which suggests a net transfer of energy from the mean flow to the fluctuations pertaining to these modes (Rajaee *et al.*, 1994). The structures attain vertical alignment at about $x/\theta_0 \simeq 35$ implying that they have attained maximum energy and indicate saturation of the fundamental instability. Until this location, the streamwise distance between subsequent structures at the same energy state is approximately equal to the wavelength of the forced fundamental instability ($\lambda_0 = 12.8 \cdot \theta_0$). Post this streamwise location, the structures remain vertically aligned but the streamwise distance between them starts to increase. In pair 1-2 (figure 5e), the ensuing structures are smaller compared to the baseline (figure 5b) initially and are all aligned vertically, implying that forcing the fundamental instability suppresses the sub-harmonic instability which is expectable. At $x/\theta_0 > 60$, the structures orient themselves with a small obtuse angle with the streamwise direction implying the natural amplification of sub-harmonic instabilities post the saturation of the fundamental instability.

The organisation of the structures is different in the mixing layer forced at $f_b = 90$ Hz. The structures in pair 1-2 (figure 5h), which correspond to fluctuations of the forced sub-harmonic frequency, are oriented with an obtuse angle with the streamwise direction. The structures tend towards a vertical alignment, but this is not achieved in the near-wake. As the fundamental instability was not simultaneously forced, the structures in pair 3-4 (figure 5i) could be a consequence of the non-linear interaction of the forced sub-harmonic instability wave with itself. While no clear structures are visible at $x/\theta_0 < 30$, downstream of this location, the observed structures have the same orientation as seen in the second mode. At $x/\theta_0 \simeq 60$, the organization of the structures resembles the occurrence of the *mode degeneration* phenomenon, where a POD structure is split into two (one in the high-velocity stream and the other in the low-velocity stream). This phenomenon is known to occur just upstream of vortex pairing in the mixing layer (Rajaee & Karlsson, 1992; Rajaee *et al.*, 1994).

The results of POD in the far-wake for both the baseline and forced mixing layer cases are presented in figure 6. As witnessed in the near-wake, in the baseline case the FFT shows no significant peaks, however fluctuations below the first sub-harmonic of the fundamental frequency are prominent (figure 6a). A similar observation can be made for the fundamental forcing case as well, and the forced $f_b = 180$ Hz is not observed either (figure 6d). The fluctuations in pair 1-2 seem to be high close to the second sub-harmonic of

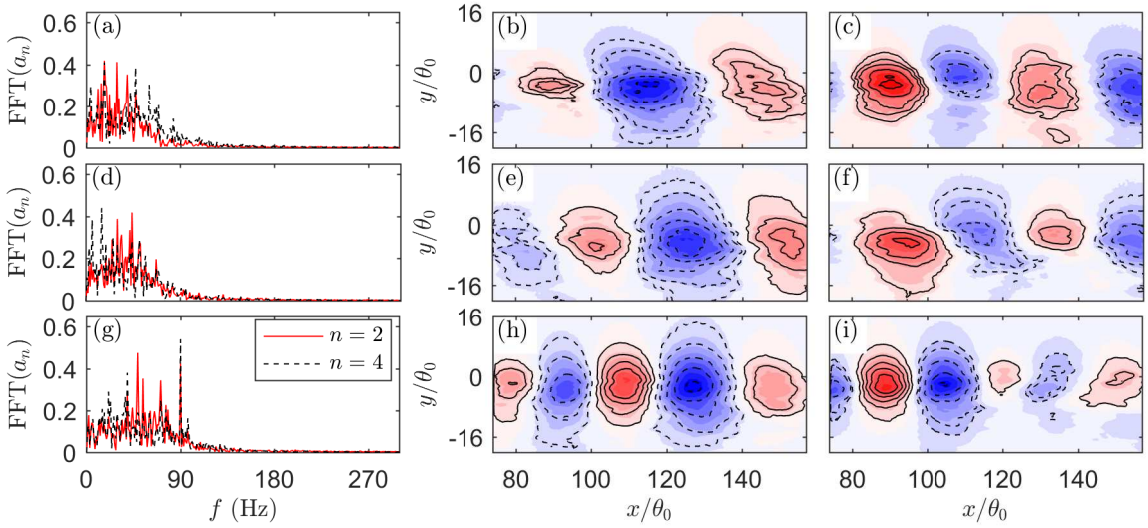

Figure 6: Far-wake POD plots. Same notation as figure 5.

the fundamental frequency. Correspondingly, the distance between subsequent structures at the same energy state in the eigenfunction (figure 6e) is about $51 \cdot \theta_0$ ($\simeq 4 \cdot \lambda_0$). As observed at the end of the near-wake ($x/\theta_0 > 60$), these structures are oriented with an obtuse angle with the streamwise direction. Furthermore, while the structures resemble those in the baseline, the angle of their orientation is lesser. This suggests that while the natural amplification of the sub-harmonic occurs, the growth of these instabilities is impeded by the fundamental forcing. In pair 3-4 as well (figure 6f), the structures resemble those in the baseline but are oriented with an obtuse angle owing to forcing the fundamental instability.

With sub-harmonic forcing, the FFT of the temporal coefficients of both mode pairs shows a peak at the forced $f_b = 90$ Hz frequency, but also at lower frequencies (figure 6g). The structures in pair 1-2 (figure 6h) are vertically aligned implying the saturation of the dominant sub-harmonic instability in this field. Additionally, the streamwise distance between structures at the same energy state is lesser compared to the baseline. While the structures in pair 3-4 are vertically aligned initially, they tend to orient themselves with an acute angle with the streamwise direction later on ($x/\theta_0 > 120$), indicating a net transfer of energy from the fluctuations corresponding to these POD modes to the mean flow.

The detection of coherent vortices and, the investigation of their dynamics and interactions due to the applied forcing is desired. For this purpose, the velocity fields were reconstructed using POD modes containing 80% of the total energy. The reconstructed vector fields of the near- and far-wake regions were stitched using a *MatLab* script. As the PIV measurement was phase-locked, these reconstructed fields can be expected to be the same as well. Hence, the phase-average of these fields was computed at eight different phases separated by 0.25π of the low frequency burst modulation for both forcing cases. The phase-average was computed with 180 and 90 snapshots for the $f_b = 180$ Hz and $f_b = 90$ Hz cases respectively. These phase-averaged vector fields are normalized and the Q-criterion (Hunt *et al.*, 1988) is applied to detect the coherent vortices. These results are presented in figure 7.

Forcing the mixing layer at $f_b = 180$ Hz (figure 7a) results in coherent vortices forming just downstream of the splitter plate. Only one instance of vortex pairing is observed (dashed black box). It begins at $x/\theta_0 \simeq 18$ and is completed by $x/\theta_0 \simeq 30$, within one burst-modulation cycle (see snapshots in figure 7a). This location is just upstream of the location where the POD structures in pair 3-4 (figures 5f) attain a vertical alignment for this forcing case. While POD structures corresponding to sub-harmonic instabilities are observed in the far-wake region (figures 6e), the strength of the spanwise vortices are seen to diminish post this amalgamation, finally resulting in their breakdown at $x/\theta_0 \simeq 70$. However, as a consequence of the high level of turbulence, this breakdown could be due to helical pairing process (Chandrsuda *et al.*, 1978), which is not observed in the current results owing to the two-dimensional measurement plane.

Sub-harmonic forcing at $f_b = 90$ Hz also results in the formation of coherent spanwise vortices just downstream of the splitter plate (figure 7b). Four instances of vortex pairing are observed within one burst-modulation cycle, further proving that the sub-harmonic acts as a catalyst for this process (Ho & Huang, 1982). Three instances of vortex pairing are depicted in figure 7b. In the first (dot-dashed red rectangle and top row of snapshots on the right), two vortices coalesce into the vortex between them, in one half-cycle of the burst modulation. It is good to note that the third vortex in this interaction is a product of an earlier pairing process. The resulting vortex convects downstream, while growing in size due to entrainment for the remaining half-cycle. It then coalesces another smaller vortex (dashed black rectangle and bottom row of snapshots on the right) in one burst-modulation cycle. This final vortex pairing is completed at about $x/\theta_0 \simeq 69$ which is just downstream of the *mode degeneration* phenomenon observed in the eigenfunction of pair 3-4 in the near-wake region (figure 5i). However, the mode degeneration phenomena corresponding to previous instances of vortex pairing in this mixing layer are not observed in the eigenfunction. This is attributed to the lack of spatial resolution of the PIV measurement of the mixing layer. Here too, the strength of the spanwise vortices begins to diminish, resulting in their breakdown at $x/\theta_0 \simeq 120$ which corresponds to the streamwise location where the fluctuations corresponding to pair 3-4 in the far-wake (fig-

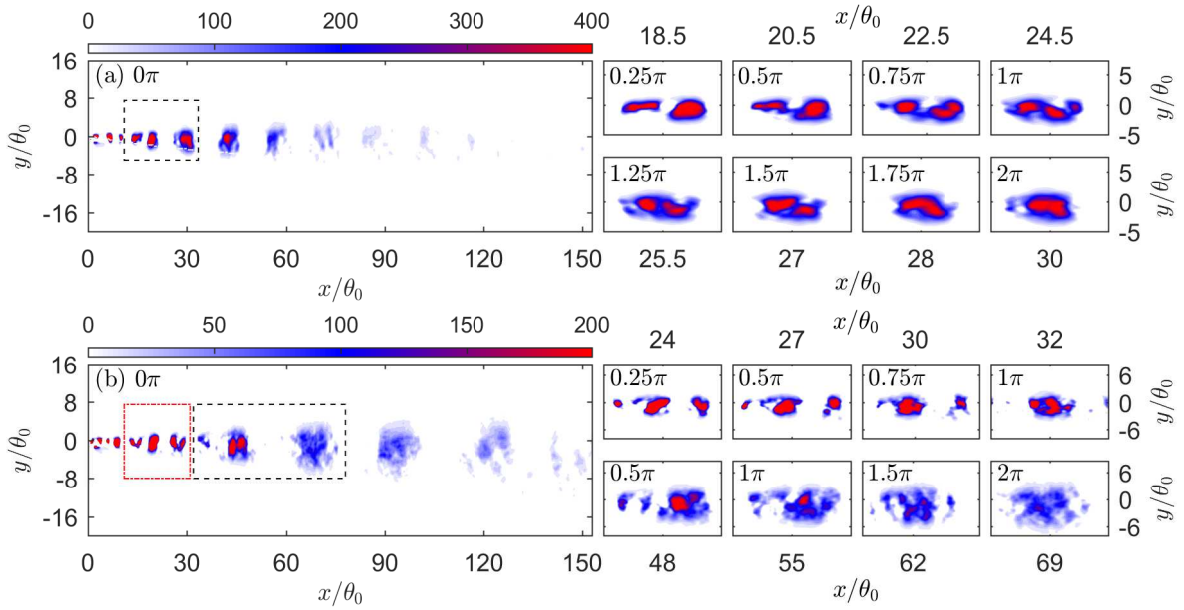

Figure 7: Second invariant of the normalized u-velocity (Q_N) computed on the phase-averaged fields of the mixing layer forced at (a) $f_b = 180$ Hz and (b) $f_b = 90$ Hz. Snapshots of vortex pairing instances for both forcing cases are also depicted.

ure 6i) begin to transfer energy to the mean flow.

4 CONCLUDING REMARKS

The presented results demonstrate that the coherent spanwise vortices in the mixing layer are influenced by the EFD forcing applied by the DBD plasma actuator. Specifically, the burst frequency modulation is observed to have an effect on the generation of spanwise vortices, the number of vortices pairing and the spatial extent of the occurrence of these instances of vortex pairing. Additionally, it also influences the location of the breakdown of these large-scale coherent vortices. However, the many instances of vortex pairing observed in these results do not articulate on the growth of the mixing layer as the momentum thickness of different cases does not show any significant difference in the measured domain. Oster & Wygnanski (1982) and Ho & Huang (1982) observed that when the vortex pairing stops, the growth of the mixing layer slows down or stops and also results in negative Reynolds stresses. Such a feature is not observed in the growth of the current (forced) mixing layers either and the Reynolds stress always remains positive (not presented here). It is suspected that given the high turbulence level in the low-velocity stream, the applied forcing is not adequate enough to achieve a high control-authority. Therefore, even though the dynamics of the ensuing vortices are affected, a significant difference in the growth rate of the mixing layer is not realized. Further research at different forcing conditions is necessary to better understand the underlying phenomenon.

ACKNOWLEDGEMENTS

This research is funded by the French Government program *Investissements d'Avenir* (LABEX INTERACTIFS, reference ANR-11-LABX-0017-01).

REFERENCES

Benard, N. & Moreau, E. 2014 Electrical and mechanical characteristics of surface ac dielectric barrier discharge plasma actuators applied to airflow control. *Exp. Fluids* **55** (11), 1–43.

Brown, G.L. & Roshko, A. 1974 On density effects and large structure in turbulent mixing layers. *J. Fluid Mech.* **64** (4), 775–816.

Chandrsuda, C., Mehta, R.D., Weir, A.D. & Bradshaw, P. 1978 Effect of free-stream turbulence on large structure in turbulent mixing layers. *J. Fluid Mech.* **85** (4), 693–704.

Ely, R. & Little, J.C. 2013 The mixing layer perturbed by a dielectric barrier discharge. p. 2753.

Ho, C.M. & Huang, L.S. 1982 Subharmonics and vortex merging in mixing layers. *J. Fluid Mech.* **119**, 443–473.

Hunt, J.C.R., Wray, A. & Moin, P. 1988 Eddies, streams, and convergence zones in turbulent flows. *Center for Turbulence Research Report* **CTR-S88**, 193–208.

Michalke, A. 1965 On spatially growing disturbances in an inviscid shear layer. *J. Fluid Mech.* **23** (3), 521–544.

Oster, D. & Wygnanski, I. 1982 The forced mixing layer between parallel streams. *J. Fluid Mech.* **123**, 91–130.

Pui, N.K. & Gartshore, I.S. 1979 Measurements of the growth rate and structure in plane turbulent mixing layers. *J. Fluid Mech.* **91** (1), 111–130.

Rajaee, M. & Karlsson, S.K.F. 1992 On the fourier space decomposition of free shear flow measurements and mode degeneration in the pairing process. *Phys. Fluids A: Fluid Dynamics* **4** (2), 321–339.

Rajaee, M., Karlsson, S.K.F. & Sirovich, L. 1994 Low-dimensional description of free-shear-flow coherent structures and their dynamical behaviour. *J. Fluid Mech.* **258**, 1–29.

Sirovich, L. 1987 Turbulence and the dynamics of coherent structures. i. coherent structures. *Qtly. Appl. Math.* **45** (3), 561–571.